Chinese Chemical Letters 32 (2021) 3793–3798

Contents lists available at ScienceDirect

Chinese Chemical Letters

journal homepage: www.elsevier.com/locate/cclet

Communication

High-performance $(NH_4)_2V_6O_{16}\cdot 0.9H_2O$ nanobelts modified with reduced graphene oxide for aqueous zinc ion batteries

Fang Hu[a,*], Yao Gu[a], Fuhan Cui[a], Guihong Song[a], Kai Zhu[b,c,*]

[a] *School of Materials Science and Engineering, Shenyang University of Technology, Shenyang 110870, China*
[b] *Key Laboratory of Superlight Materials and Surface Technology of Ministry of Education, College of Materials Science and Chemical Engineering, Harbin Engineering University, Harbin 150010, China*
[c] *Department of Mechanical Engineering, the Hong Kong Polytechnic University, Hong Kong 999077, China*

ARTICLE INFO

Article history:
Received 25 February 2021
Revised 26 March 2021
Accepted 16 April 2021
Available online 26 April 2021

Keywords:
$(NH_4)_2V_6O_{16}\cdot 0.9H_2O$@RGO
Nanobelts
Aqueous Zn-ion batteries
Electrochemical performance
Reaction mechanism

ABSTRACT

Ammonium vanadate has been considered as a competitive high-performance cathode material for aqueous Zn-ion batteries. However, it still suffers from insufficient rate capability and poor cyclability due to the low electronic conductivity. Herein, $(NH_4)_2V_6O_{16}\cdot 0.9H_2O$ nanobelts with reduced graphene oxide (RGO) modification are synthesized by one-step hydrothermal reaction. Benefiting from the addition of RGO, an excellent electrochemical performance of $(NH_4)_2V_6O_{16}\cdot 0.9H_2O$@RGO nanobelts can be obtained. The $(NH_4)_2V_6O_{16}\cdot 0.9H_2O$@RGO displays a high-rate capacity and a high energy density of 386 Wh/kg at 72 W/kg. In particular, after 1000 cycles at 5 A/g, the capacity remains at 322 mAh/g with 92.8% capacity retention. In addition, the key reaction mechanisms of reversible Zn^{2+}insertion/extraction in $(NH_4)_2V_6O_{16}\cdot 0.9H_2O$@RGO are clarified.

Aqueous rechargeable batteries (ARBs) have received much attention owing to high ionic conductivity, high safety, low cost and environment-friendly [1,2]. Among the ARBs, zinc ion batteries (ZIBs) are particularly attractive owing to the inherent advantages of Zn metal: abound resources, the high theoretical capacity of 820 mAh/g, and low redox potential of −0.76 V (*vs.* SHE) [3,4]. However, the strong positive polarity of Zn^{2+} and its large atomic mass limit the choices of suitable cathode compared to the Li-ion and Na-ion batteries [5,6].

As one of the most promising cathodes for ZIBs, the vanadium-based compound with the open framework, such as VO_2 [7,8], $Zn_{0.25}V_2O_5\cdot nH_2O$ [9], $H_2V_3O_8$ [10,11], $Na_2V_6O_{16}\cdot nH_2O$ [12,13] and $NH_4V_4O_{10}$ [14,15], attracts many scientists to study because of its higher specific capacity, higher energy density and faster charge-discharge capability than manganese-based compound, Prussian blue or organic redox-active compound [16,17]. However, the cycling and rate performance of vanadium-based compounds still need to be improved due to the poor electrical conductivity and structure collapse during the Zn^{2+} insertion/extraction process. For instance, Xiong *et al.* prepared layered $(NH_4)_2V_6O_{16}\cdot 1.5H_2O$ nanobelts with a high specific capacity of 479 mAh/g at the current density of 100 mA/g. But the capacity decreases from 284.6 mAh/g to 209.6 mAh/g after 1000 cycles at 3 A/g [18].

Introducing carbon materials is an effective method to enhance the electron transport and the electrochemical utilization of the electrode materials [19,20]. In this work, $(NH_4)_2V_6O_{16}\cdot 0.9H_2O$ nanobelts with reduced graphene oxide (RGO) modification are synthesized by a one-step hydrothermal reaction. Thanks to the addition of RGO, an excellent electrochemical performance of $(NH_4)_2V_6O_{16}\cdot 0.9H_2O$@RGO nanobelts can be achieved. The $(NH_4)_2V_6O_{16}\cdot 0.9H_2O$@RGO displays a high specific capacity of 537 mAh/g at 0.1 A/g and excellent rate capability. In particular, after 1000 cycles at 5 A/g, the capacity remains at 322 mAh/g with 92.8% capacity retention.

In a typical procedure, $(NH_4)_2V_6O_{16}\cdot 1.4H_2O$ nanobelts was prepared by a facile hydrothermal method. Firstly, 0.5 g NH_4VO_3 powder was dispersed in 25 mL deionized water. Then, 0.2 mL phosphoric acid (H_3PO_4, 88%, pH 1.5) was introduced to the solution, and a wine-red clarified solution was formed through the string for 15 min. Finally, the solution was transferred into a 50 mL Teflon-lined stainless autoclave and kept for 72 h at 130 °C. The product was collected by washing with deionized water three times and ethanol once. The powders were dried in a vacuum oven for 24 h at 60 °C.

The $(NH_4)_2V_6O_{16}\cdot 0.9H_2O$ nanobelts with reduced graphene oxide modification were obtained by adding a concentration of

---

* Corresponding authors.
E-mail addresses: hufang25@126.com (F. Hu), kzhu@hrbeu.edu.cn (K. Zhu).

https://doi.org/10.1016/j.cclet.2021.04.032

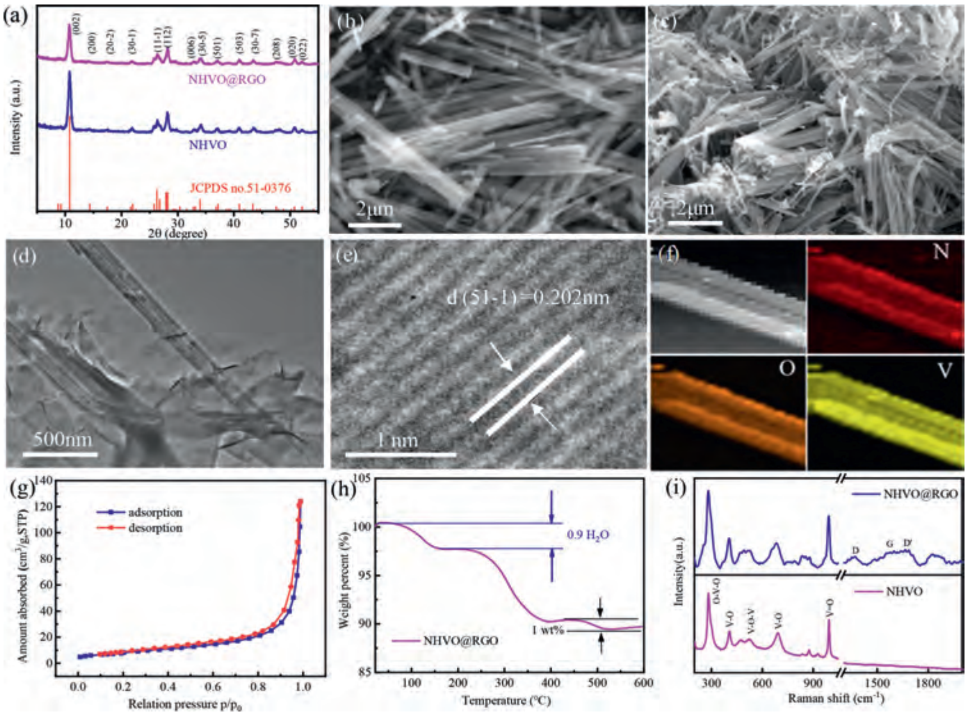

Fig. 1. (a) XRD patterns of NHVO and NHVO@RGO. (b, c) SEM images of NHVO and NHVO@RGO. (d) TEM image of NHVO@RGO. (e) HRTEM images of NHVO@RGO. (f) Elemental mapping images of NHVO nanobelt. (g) Nitrogen adsorption-desorption isotherms curves of NHVO@RGO. (h) TG of NHVO@RGO. (i) Raman of NHVO and NHVO@RGO.

1 mg/mL graphene oxide (GO) solution into the 25 mL deionized water, and the following step was same as the above-mentioned steps.

The as-prepared samples were characterized by X-ray diffraction (XRD) analysis on an X-ray diffractometer equipped with Cu K_α radiation (λ = 0.1542 nm). The morphologies and microstructure of the samples were characterized by scanning electron microscopy (SEM, Hitachi-4800) and transmission electron microscopy (TEM, JEM-2100 PLUS). The elemental composition and chemical bond valence of the cathode material surface were measured by X-ray photoelectron spectroscopy (XPS). *In-situ* XRD patterns of the samples were recorded using a Bruker D8 Advance diffractometer.

The working electrode was prepared *via* mixing active materials, acetylene black, and polytetrafluoroethylene emulsion in a weight ratio of 7:2:1. Then, the mixture was rolled into uniform thickness and pressed on conductive carbon paper with a diameter of 1 cm. The average mass loading of the active materials was about 1.3 mg/cm^2. The electrolyte was 3 mol/L $Zn(CF_3SO_3)_2$ solution. An electrochemical workstation (Bio-Logic VSP-300) was used to test the electrochemical properties and electrochemical reaction kinetics analysis of the coin cells, including cyclic voltammetry (CV), electrochemical impedance spectra (EIS), and galvanostatic intermittent titration technique (GITT) measurement. Multichannel galvanostatic (Neware CT-4000) testers were used to perform galvanostatic charge-discharge cycling.

XRD patterns of pure $(NH_4)_2V_6O_{16}\cdot 1.5H_2O$ (denoted as NHVO) and $(NH_4)_2V_6O_{16}\cdot 1.5H_2O$@RGO (denoted as NHVO@RGO) are shown in Fig. 1a. Both of the diffraction peaks are well-matched with the monoclinic $(NH_4)_2V_6O_{16}\cdot 1.5H_2O$ (JCPDS No. 51–0376) [21,22], and impurities are not detected. Figs. 1b and c show the SEM images of NHVO and NHVO@RGO, respectively. Both of NHVO and NHVO@RGO present belts-like morphology with lengths above 5 μm. It is hard to observe the graphene from the SEM image, which will be discussed later. However, the nanobelt clustering of NHVO@RGO is more serious than NHVO, which could be due to the electrostatic interaction of RGO with NHVO nanobelts. In addition, from the TEM image of NHVO@RGO in Fig. 1d, it can be seen that the nanobelt is about 200 nm in width and wrapped with RGO. HRTEM in Fig. 1e displays the lattice fringes of 0.202 nm corresponding to $(51\bar{1})$ planes of NHVO. The element mappings (Fig. 1f) demonstrated that the elements (N, V and O) are uniform-distributed in the NHVO nanobelt. The BET surface area of NHVO@RGO in Fig. 1g is 27.8 m^2/g, which favors increasing the interface area between the electrode and electrolyte and improving the electrochemical performance of NHVO@RGO.

To further understand the characterizations of the NHVO@RGO, thermogravimetric analysis (TG) measurement was carried out to estimate the content of water and graphene in the NHVO and NHVO@RGO, respectively. As shown in Fig. 1h and Fig. S1 (Supporting information), the contents of water were 2.3 wt% and 3 wt%, respectively, corresponding to 1.4 and 0.9 water molecules per formula unit. Therefore, NHVO and NHVO@RGO should be defined to $(NH_4)_2V_6O_{16}\cdot 1.4H_2O$ and $(NH_4)_2V_6O_{16}\cdot 0.9H_2O$@RGO, respectively. When annealed to 400 °C, a large weight loss happens, which can be attributed to the decomposition reaction from $(NH_4)_2V_6O_{16}$ to V_2O_5 phase with the volatilization of NH_3 and H_2O. In addition, a weight loss (~1 wt%) of NHVO@RGO occurs from 400 °C to 500 °C, it can be assigned to the content of RGO. Fig. 1i shows the Raman scattering spectra of NHVO and NHVO@RGO, respectively. Between the wavelength range of 200–1000 cm^{-1}, several obvious peaks of NHVO located at 281, 407, 526, 690 and 992 cm^{-1} could be corresponded to the bending vibrations of the O-V-O, V-O and V-O-V bonds and the stretching vibration of V-O and V=O bonds, respectively [23]. In the high-wavenumber region, the peaks located at 1364, 1573 and 1665 cm^{-1} correspond to D, G and D′ bands of single layer graphene [24]. Therefore, we can sure the NHVO is wrapped with RGO, even though it is hard to observe from the result of SEM.

The electrochemical performance of NHVO@RGO is systematically investigated in Fig. 2. CV curves of NHVO@RGO and NHVO in the initial three cycles at a scan rate of 0.1 mV/s are shown in

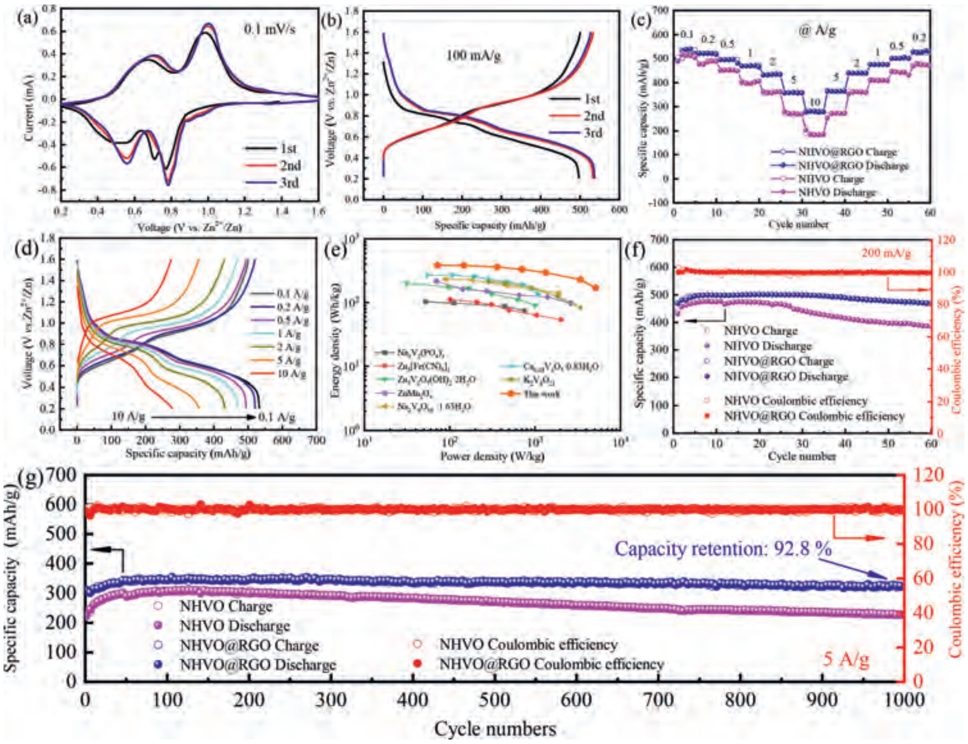

Fig. 2. (a) CV curves of NHVO@RGO collected at a scan rate of 0.1 mV/s. (b) The first three discharge-charge profiles of NHVO@RGO at a current density of 100 mA/g. (c) Rate performances of NHVO and NHVO@RGO. (d) The discharge and charge curves of a NHVO@RGO electrode at various current densities in the voltage range 0.2–1.6 V. (e) Ragone plot of NHVO@RGO//Zn compared with other reported cathode materials. (f, g) Cyclic performances of NHVO and NHVO@RGO for 60 cycles at 200 mA/g and for 1000 cycles at 5 A/g, respectively.

Fig. 2a and Fig. S2 (Supporting information), respectively. In the cathodic scan at the first cycle, there are three oxidation peaks at about 0.77, 0.71 and 0.52 V, indicating a multi-step electrochemical embedding process of Zn^{2+}. However, in the anode scan, only two reduction peaks at about 0.66 and 0.97 V are observed, demonstrating an irreversible phase transformation. After the first cycle, all the CV curves are mostly overlapped, implying high reversibility of Zn^{2+} insertion and extraction process. The main redox peaks at 0.78 V/0.98 V can be attributed to the V^{5+}/V^{4+} redox couple, and 0.56 V/0.71 V represents the V^{4+}/V^{3+} redox couple [12]. The discharge-charge curves of NHVO@RGO and NHVO in the initial three cycles at the current density of 100 mA/g are shown in Fig. 2b and Fig. S3 (Supporting information), respectively. Both of the initial discharge curves are different from the back, which is consistent with the results of CV. A high discharge capacity of NHVO@RGO can be up to 540 mAh/g after three cycles. Compared to that of NHVO (463 mAh/g), the increased capacity about 80 mAh/g of NHVO@RGO can be assigned to the addition of RGO, which enhances the active sites [25]. To make sure RGO has not provided those extra capacity, the electrochemical performance of RGO is also investigated in Fig. S4 (Supporting information). The initial discharge capacity is about 25 mAh/g average specific capacity of RGO is less than 20 mAh/g at the current density of 200 mA/g. Therefore, the RGO does not provide the NHVO@RGO electrode much capacity. Fig. 2c shows the rate performance of NHVO and NHVO@RGO at the various current density from 0.1 A/g to 10 A/g. Compared to NHVO, NHVO@RGO cathode delivers high capacities of 536, 522, 496, 469, 435, 358 and 282 mAh/g at the current densities of 0.1, 0.2, 0.5, 1, 2, 5 and 10 A/g, respectively. When the current is gradually back to 0.2 A/g, an average capacity of 527 mAh/g can be obtained, demonstrating an excellent rate performance and reversibility of NHVO@RGO electrode during the Zn^{2+} insertion/extraction process. The corresponded discharge-charge profiles of NHVO@RGO electrode at the above various current density are shown in Fig. 2d, suggesting that the polarization between the discharging and charging curve increases with the raise of the current density. To evaluate the practical potential of NHVO@RGO cathode for ZIBs, Ragone plots of NHVO@RGO and other cathode materials (based on the active mass of the cathode materials) are shown in Fig. 2e. The energy density and power density can be calculated by the following equations (Eqs. 1 and 2) [26]:

$$\text{Energy density (Wh/kg)} = \frac{QU}{m} \tag{1}$$

$$\text{Power density (W/kg)} = \frac{iU}{m} \tag{2}$$

where Q is the discharge capacity (Ah); U, i and m denote the main operating voltage (V), the discharge currents (A) and the mass of the active material (kg), respectively. When the power density is 72 W/kg, the energy density of NHVO@RGO can be up to 386 Wh/kg. Even, the power density is up to 5126 W/kg, the energy density of NHVO@RGO remains at a high value of 169 Wh/kg. The values of the energy density and power density of NHVO@RGO is larger than that of reported materials, such as $Na_3V_2(PO_4)_3$ [27], $Na_2V_6O_{16}\cdot1.63H_2O$ [28], $Zn_3[Fe(CN)_6]_2$ [29], $Ca_{0.24}V_2O_5\cdot0.83H_2O$ [30] and others [31–33].

The NHVO@RGO cathode also demonstrates superior cyclic stability as shown in Fig. 2f. An initial discharge capacity of 468 mAh/g can be obtained at the current density of 0.2 A/g. After 10 cycles of activation, the maximum capacity can be up to 500 mAh/g. After 50 cycles, the capacity remains 469 mAh/g with a capacity retention of 93.8%. In contrast, the capacity of the NHVO cathode reduces from the maximum value of 476 mAh/g to 387 mAh/g, corresponding to a capacity retention of 81.3%.

Furthermore, at a high current density of 5 A/g, NHVO@RGO cathode shows a maximum capacity of 347 mAh/g after 60 cycles of activation. After 1000 cycles, the capacity can remain at

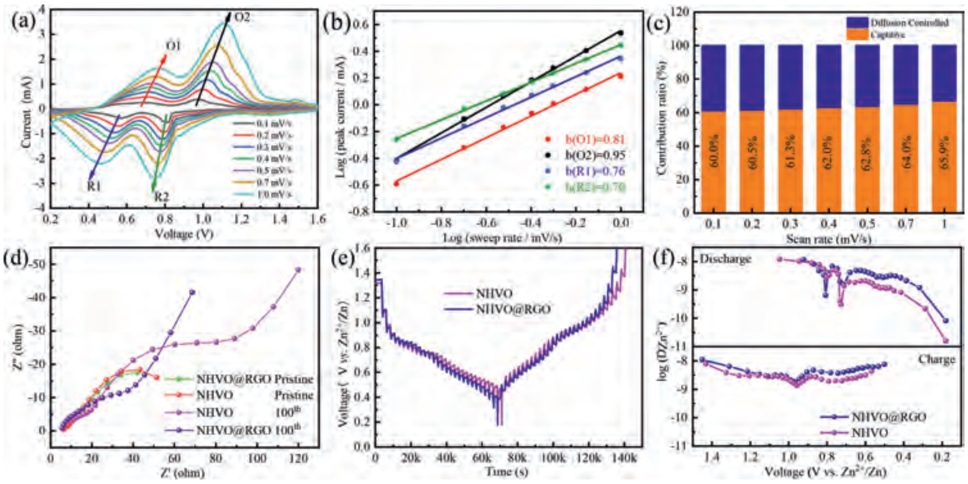

Fig. 3. (a) CV curves of NHVO@RGO at different scan rates. (b) Log (*i*, current) versus log (mV, scan rate) plots at specific current. (c) Calculated capacitive contributions for NHVO@RGO at different scan rates. (d) The impedance spectrums for NHVO and NHVO@RGO. (e) GITT profiles of NHVO and NHVO@RGO. (f) Diffusion coefficient at various states during GITT measurement.

322 mAh/g with 92.8% capacity retention. However, the NHVO only presents a capacity retention of 74.4%. Compared to other ammonium vanadate materials as cathodes for AZIBs in Table S1 (Supporting information), the NHVO@RGO electrode also shows higher rate capability and excellent cycle performances.

The kinetic properties of NHVO@RGO during Zn^{2+} insertion/extraction are further investigated. Fig. 3a displays the CV profiles of NHVO@RGO electrode from 0.1 mV/s to 1.0 mV/s. The charge transfer behavior can be determined according to the relationship between the measured current (i) and scan rate (n) by the following equation (Eq. 3) [10]:

$$i = av^b \tag{3}$$

where a and b are adjustable parameters, in which the latter varies between 0.5 and 1. The b-value of 0.5 indicates a diffusion-limited process, while b closing to 1.0 implies a capacitive process. After calculated in Fig. 3b, the b values of peaks O1, O2, R1 and R2 are 0.81, 0.95, 0.76 and 0.70, respectively. It implies the kinetics of Zn^{2+} in NHVO@RGO are main capacitive process and not significantly influenced by the diffusion process, which is favor to improve the rate capability of NHVO@RGO. To quantitative analyze the contribution ratio between diffusion-controlled and capacitive behaviors, the equation can be further described as following (Eq. 4) [34]:

$$i = k_1v + k_2v^{1/2} \tag{4}$$

where k_1v represents the capacitive behaviors and $k_2v^{1/2}$ denotes the diffusion-limited contribution, respectively. For instance, there is a 63% capacitive contribution of the total capacity at the scan rate of 0.5 mV/s, as shown in Fig. S5 (Supporting information). With the scan rates increased from 0.1 mV/s to 1 mV/s in Fig. 3c, the capacitive contribution ratios increased from 60% to 65.9%, indicating a tendency that the capacitive charge storage would play an important role in the total capacitance of NHVO@RGO when the rate increased.

To account for the extraordinary high-rate performance, the EIS result of the NHVO and NHVO@RGO cells are recorded in Fig. 3d and Table S2 (Supporting information). Based on the equivalent circuit and quantitative fitting of the EIS spectra, the charge-transfer resistance (R_{ct}) of NHVO@RGO is about 37 Ω, which is lower than that of NHVO (58.3 Ω). It confirms that the RGO enhanced the charge transfer kinetics of the NHVO electrode. The diffusion coefficient of Zn^{2+} during the front two cycles were carried out by GITT in Fig. 3e. The data of NHVO and NHVO@RGO was collected at a current density of 100 mA/g in the discharge state for 10 min and rest intervals of 30 min. The Zn^{2+} diffusion coefficient in the NHVO@RGO electrode can be calculated by the following equation (Eq. 5) [35]:

$$D = \frac{4}{\pi\tau}\left(\frac{m_B V_M}{M_B S}\right)^2\left(\frac{\Delta E_s}{\Delta E_\tau}\right)^2 \tag{5}$$

where m_B, V_M, M_B and S denote the mass, molar volume, molecular mass of the active material, and the active surface area of the electrode, respectively. ΔE_s and ΔE_τ represent the steady-state potential change by the current pulse and the potential change during the constant current pulse after eliminating the *iR* drop, respectively. As shown in Fig. 3f, the minimal values at about 0.8 V correspond to the voltage plateaus of the discharge process. The calculated ionic diffusion coefficients of NHVO@RGO are between 1.1×10^{-8} m^2/s and 6.1×10^{-10} cm^2/s, which is higher than that of NHVO. It confirms the better electrochemical kinetic properties of NHVO@RGO than NHVO. It can be attributed to that the more active sites of NHVO@RGO than NHVO provide more pathways of Zn^{2+} transport and improve the Zn^{2+} diffusion coefficients.

To investigate the structure evolution during the discharge-charge process, *in-situ* XRD spectra of the NHVO@RGO electrode was performed at 100 mA/g during the front two cycles in Fig. 4a and Fig. S6 (Supporting information). The main (002) peak shifts slightly from $2\theta = 10.8°$ to 11.0° in the first discharge process corresponding to the reduction of interlayer distance from 0.82 nm to 0.8 nm, which demonstrates the electrostatic intercalation between the inserted Zn^{2+} and $(V_6O_{16})^{2-}$ layers [36]. Meanwhile, the $(10\bar{1})$ and $(20\bar{2})$ peaks of NHVO at $2\theta = 8.5°$ and 17° disappear gradually and a new series peaks of the second phase at $2\theta = 6.5°$, 13.1°, 19.6°, 26.3° and 33.0° appears. It can be assigned to the set of (00l) reflections of the layered $Zn_xV_2O_5{\cdot}nH_2O$ phase, which is similar to the case in previously reported studies [37,38]. The second phase might originate from the insertion of hydrated $Zn(H_2O)_6{}^{2+}$ and react with the surface of the NHVO framework, resulting in the formation of the $Zn_xV_2O_5{\cdot}nH_2O$ phase. After charging, the (002) peak of NHVO is shifted back to 10.85°, corresponding to the Zn^{2+} extraction. The $(10\bar{1})$ and $(20\bar{2})$ peaks appear, and the $Zn_xV_2O_5{\cdot}nH_2O$ phase disappears gradually, indicating the reversibility of phase transformation between NHVO and $Zn_xV_2O_5{\cdot}nH_2O$. Subsequently, the (002) peak of NHVO@RGO remains during the second cycle, and $Zn_xV_2O_5{\cdot}nH_2O$ phase appears in the discharge and disappears

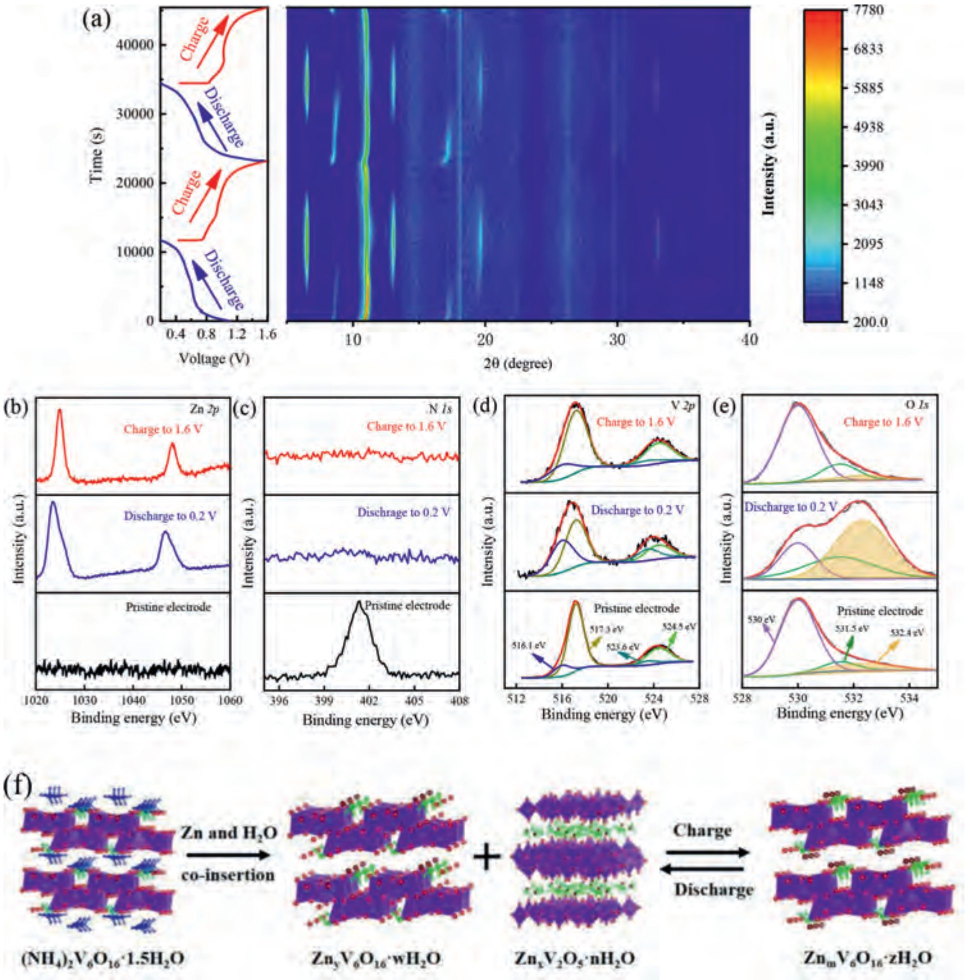

Fig. 4. (a) *In-situ* XRD patterns of NHVO@RGO obtained in the first two cycles at the applied current density of 100 mA/g. (b-e) *Ex-situ* high resolution XPS spectrums of Zn 2p, N 1s, V 2p and O 1s at different discharge/charge states of NHVO@RGO. (f) Schematic illustration of the reaction mechanism of NHVO.

in the charging process, demonstrating the stable framework of NHVO.

To better understand the mechanism of Zn ion storage in NHVO@RGO, *ex-situ* XPS was carried out. As shown in Fig. 4b, no Zn signal can be detected in the initial electrode. After discharge to 0.2 V, two strong peaks located at 1023.2 eV and 1046.4 eV appear, declaring the insertion of Zn^{2+} into the layered NHVO. After charging, the two peaks with shifts and comparatively weak intensities can also be observed. In general, the irreversible ion extraction would result in charge-capacity fading. However, there is no capacity fading in the first cycle with ~100% coulombic efficiency (as depicted in Fig. 2b). Fig. 4c shows the evolution of XPS spectra of N 1s during the Zn^{2+} intercalation/extraction process. A signal located at 401.3 eV corresponding to the N 1s in the pristine electrode. However, after discharge and charge over, no peaks are found. Combined with the result of XPS spectra of Zn 2p, it suggests that the Zn^{2+} intercalation irreversibly displaces with NH_4^+ in the discharge-charge process and acts as a new pillar to stabilize the framework of NHVO. To further confirm the above displacement mechanism, *ex-situ* FTIR was carried out in Fig. S7 (Supporting information). In the initial electrode, an obvious broad peak located at about 3130 cm^{-1} can be attributed to the asymmetric stretching vibration of N–H from NH_4^+ [39]. When discharged to 0.2 V and charged to 1.6 V, the intensity of the broad peak is obviously decreased, suggesting the NH_4^+ was indeed extracted from the structure of NHVO. In the V 2p region (Fig. 4d), the peak of pristine electrode is composed of V^{4+} (516.1 eV) and V^{5+} (517.3 eV) [40]. After discharging, the intensity of the V^{4+} signal became strong, and the V^{5+} signal becomes weak, indicating the reduction of V^{5+} with the Zn^{2+} intercalation. When the cell is charged fully, the intensity of the V^{4+} and V^{5+} signal is back to the initial state, indicating high reversibility during the cycling. In addition, three peaks of O 1s (Fig. 4e) located at 529.9, 531.5, and 532.2 eV can be assigned to O^{2-}, OH^- and H_2O molecules, respectively [41]. When discharged to 0.2 V, the peak of H_2O strengthens, corresponding to the formation of the $Zn_xV_2O_5{\cdot}nH_2O$ phase. After charging, the H_2O signal is retained, which is also in accordance with the *in-situ* XRD result.

Based on the above analysis, the structure evolution during the Zn^{2+} insertion/extraction process can be graphically summarized to illustrate the phase transformation. As shown in Fig. 4f, with the co-insertion of Zn^{2+} and H_2O molecules into the layer of $(NH_4)_2V_6O_{16}{\cdot}1.5H_2O$, NH_4^+ was displaced by the Zn^{2+}, and the phase are transformed to $Zn_yV_6O_{16}{\cdot}nH_2O$ and a new $Zn_xV_2O_5{\cdot}nH_2O$ phase on the surface [42]. After charging, the Zn ions are extracted from the new $Zn_xV_2O_5{\cdot}nH_2O$ phase and $Zn_yV_6O_{16}{\cdot}nH_2O$, and $Zn_mV_6O_{16}{\cdot}nH_2O$ phase is formed. In the subsequent cycles, the $Zn_mV_6O_{16}{\cdot}nH_2O$ phase is reversibly transformed to $Zn_yV_6O_{16}{\cdot}nH_2O$ and $Zn_xV_2O_5{\cdot}nH_2O$ phase with Zn^{2+} insertion.

In conclusion, $(NH_4)_2V_6O_{16}{\cdot}0.9H_2O$ nanobelts with reduced graphene oxide modification have been synthesized by a one-step hydrothermal reaction. When used in aqueous Zn//$(NH_4)_2V_6O_{16}\cdot0.9H_2O$@RGO cell, the cathode demonstrates significantly enhanced electrochemical performance with a high energy density of 386 Wh/kg at 72 W/kg and excellent long-term cycles (92.8% capacity retention after 1000 cycles at 5A/g). The findings presented in our work exhibit the promising applications of this material as the prospective cathode of ZIBs with ultrahigh power density.

Declaration of competing interest

The authors declare that they have no known competing financial interests or personal relationships that could have appeared to influence the work reported in this paper.

Acknowledgments

This work was partly supported by the National Natural Science Foundation of China (No. 51772193), China Postdoctoral Science Foundation (No. 2019T120254) and Hong Kong Scholar Program (No. XJ2019024).

Supplementary materials

Supplementary material associated with this article can be found, in the online version, at doi:10.1016/j.cclet.2021.04.032.

References

[1] Y.L. Liang, H. Dong, D. Aurbach, et al., Nat. Energy 5 (2020) 646–656.
[2] X.S. Xie, S.Q. Liang, J.W. Gao, et al., Energ. Environ. Sci. 13 (2020) 503–510.
[3] L.E. Blanc, D. Kundu, L.F. Nazar, Joule 4 (2020) 771–799.
[4] S.F. Chen, Y.F. Zhang, H.B. Geng, et al., J. Power Sources 441 (2019) 227192.
[5] J.T. Xu, S.X. Dou, H.K. Liu, L.M. Dai, Nano Energy 2 (2013) 439–442.
[6] P.K. Nayak, L.T. Yang, W. Brehm, et al., Angew. Chem. Int. Ed. 57 (2018) 102–120.
[7] X. Dai, F. Wan, L.L. Zhang, H.M. Cao, Z.Q. Niu, Energy Storage Mater. 17 (2019) 143–150.
[8] K.Y. Zhu, T. Wu, S.C. Sun, et al., Energy Stor. Mater. 29 (2020) 60–70.
[9] D. Kundu, B.D. Adams, V. Duffort, S.H. Vajargah, L.F. Nazar, Nat. Energy 1 (2016) 16119.
[10] P. He, Y.L. Quan, X. Xu, et al., Small 13 (2017) 1702551.
[11] Q. Pang, C.L. Sun, Y.H. Yu, et al., Adv. Energy Mater. 8 (2018) 1800144.
[12] F. Hu, D. Xie, D.P. Zhao, et al., J. Energy Chem. 38 (2019) 185–191.
[13] V. Soundharrajan, B. Sambandam, S. Kim, et al., Nano Lett. 18 (2018) 2402–2410.
[14] H. Wang, R.P. Jing, J.R. Shi, et al., J. Alloys Compd. 858 (2021) 158380.
[15] B.Y. Tang, J. Zhou, G.Z. Fang, et al., J. Mater. Chem. A 7 (2019) 940–945.
[16] Y.J. Zhang, Y. Wang, L. Lu, C.W. Sun, D.Y.W. Yu, J. Power Sources 484 (2021) 229263.
[17] T. Xiong, Y.X. Zhang, W.S.V. Lee, J.M. Xue, Adv. Energy Mater. 10 (2020) 2001769.
[18] X. Wang, B.J. Xi, Z.Y. Feng, et al., J. Mater. Chem. A 7 (2019) 19130–19139.
[19] Y.S. Lai, Y.M. Dai, J.M. Jehng, Catal. Today 325 (2019) 41–46.
[20] M. Endo, C. Kim, K. Nishimura, et al., Carbon 38 (2000) 183–197.
[21] H.Y. Li, L. Wang, C. Wei, et al., Mater. Technol. 30 (2015) A109–A114.
[22] N. Wang, W. Chen, L. Mai, et al., J. Solid State Chem. 181 (2008) 652–657.
[23] M. Florea, R.S. Marin, F.M. Palasanu, F. Neatu, V.I. Pârvulescu, Catal. Today 254 (2015) 29–35.
[24] C. Nethravathi, B. Viswanath, J. Michael, M. Rajamath, Carbon 50 (2012) 4839–4846.
[25] F.H. Cui, J. Zhao, D.X. Zhang, et al., Chem. Eng. J. 390 (2020) 124118.
[26] S.L. Chou, J.Z. Wang, H.K. Liu, et al., J. Phys. Chem. C 115 (2011) 16220–16227.
[27] P. Hu, T. Zhu, X.P. Wang, et al., Nano Energy 58 (2019) 492–498.
[28] P. Hu, T. Zhu, X.P. Wang, et al., Nano Lett 18 (2018) 1758–1763.
[29] L.Y. Zhang, L. Chen, X.F. Zhou, Z.P. Liu, Sci. Rep. 5 (2015) 18263.
[30] C. Xia, J. Guo, P. Li, X.X. Zhang, H.N. Alshareef, Angew. Chem. Int. Ed. 57 (2018) 3943–3948.
[31] B.Y. Tang, G.Z. Fang, J. Zhou, et al., Nano Energy 51 (2018) 579–587.
[32] L.L. Chen, Z.H. Yang, H.G. Qin, et al., J. Power Sources 425 (2019) 162–169.
[33] Y.Y. Lu, T.Y. Zhu, W. Bergh, et al., Angew. Chem. Int. Ed. 59 (2020) 17004–17011.
[34] J. Wang, J. Polleux, J. Lim, et al., J. Phys. Chem. C 111 (2007) 14925–14931.
[35] P.F. Wang, K. Zhu, K. Ye, et al., J. Colloid Interface Sci. 561 (2020) 203–210.
[36] H.M. Jiang, Y.F. Zhang, L. Xu, et al., Chem. Eng. J. 382 (2020) 122844.
[37] M.Y. Yan, P. He, Y. Chen, et al., Adv. Mater. 30 (2018) 1703725.
[38] V. Petkov, P.N. Trikalitis, E.S. Bozin, et al., J. Am. Chem. Soc. 124 (2002) 10157–10162.
[39] X. Wang, B.J. Xi, Z.Y. Feng, et al., J. Mater. Chem. A 7 (2019) 19130–19139.
[40] Y.F. Zhang, C.X. Chen, W.B. Wu, et al., Ceram. Int. 39 (2013) 129–141.
[41] H.M. Jiang, Y.F. Zhang, Z.H. Pan, et al., Mater. Chem. Front 4 (2020) 1434–1443.
[42] G.Z. Yang, T.Y. Wei, C.X. Wang, ACS Appl. Mater. Interfaces 10 (2018) 35079–35089.